

1 Detection of slow slip events using wavelet
2 analysis of GNSS recordings

3 Ariane Ducellier¹, Kenneth C. Creager², and David A. Schmidt²

4 ¹Corresponding author. University of Washington, Department of
5 Earth and Space Sciences, Box 351310, 4000 15th Avenue NE
6 Seattle, WA 98195-1310, ariane.ducellier.pro@gmail.com

7 ²University of Washington, Department of Earth and Space
8 Sciences

9 **Key points**

- 10 • We use a wavelet-based signal processing method to detect transients in
11 GNSS data, such as slow slip events.
- 12 • In Northern Cascadia, there is good **agreement** between detections of
13 slow slip using GNSS data and using tremor data.
- 14 • The method **can** be applied **as a starting point to identify slow slip**
15 **without prior information. New Zealand is shown as on example.**

₁₆ **Abstract**

₁₇ In many places, tectonic tremor is observed in relation to slow slip and can
₁₈ be used as a proxy to study slow slip events of moderate magnitude where
₁₉ surface deformation is hidden in Global Navigation Satellite System (GNSS)
₂₀ noise. However, in subduction zones where no clear relationship between tremor
₂₁ and slow slip occurrence is observed, these methods cannot be applied, and we
₂₂ need other methods to be able to better detect and quantify slow slip. Wavelets
₂₃ methods such as the Discrete Wavelet Transform (DWT) and the Maximal
₂₄ Overlap Discrete Wavelet Transform (MODWT) are mathematical tools for
₂₅ analyzing time series simultaneously in the time and the frequency domain by
₂₆ observing how weighted differences of a time series vary from one period to the
₂₇ next. In this paper, we use wavelet methods to analyze GNSS time series and
₂₈ seismic recordings of slow slip events in Cascadia. We use detrended GNSS
₂₉ data, apply the MODWT transform and stack the wavelet details over several
₃₀ nearby GNSS stations. As an independent check on the timing of slow slip
₃₁ events, we also compute the cumulative number of tremor in the vicinity of the
₃₂ GNSS stations, detrend this signal, and apply the MODWT transform. In both
₃₃ time series, we can then see simultaneous waveforms whose timing corresponds
₃₄ to the timing of slow slip events. We assume that there is a slow slip event
₃₅ whenever there is a positive peak followed by a negative peak in the wavelet
₃₆ signal. We verify that there is a good **agreement** between slow slip events
₃₇ detected with only GNSS data, and slow slip events detected with only tremor
₃₈ data for northern Cascadia. The wavelet-based detection method effectively
₃₉ detects events of magnitude higher than 6 as determined by independent event
₄₀ catalogs (e.g. (Michel et al., 2019)). As a demonstration of using the wavelet
₄₁ analysis in a region without significant tremor, we also analyze GNSS data from
₄₂ New Zealand and detect slow slip events that are spatially and temporally close

⁴³ to those detected previously by other studies.

⁴⁴ 1 Introduction

⁴⁵ Slow slip events are new phenomena discovered in the last two decades in many
⁴⁶ subduction zones thanks to recordings of the displacement of Earth's surface by
⁴⁷ dense Global Navigation Satellite System (GNSS) networks (Vergnolle et al.,
⁴⁸ 2010; Schmidt and Gao, 2010; Jiang et al., 2012; Wallace et al., 2012). As with
⁴⁹ ordinary earthquakes, slow slip events represent slip on a fault, for instance
⁵⁰ the plate boundary between a tectonic plate subducting under another tectonic
⁵¹ plate. However, they take a much longer time (several days to several years) to
⁵² happen relative to ordinary earthquakes. They have a relatively short recurrence
⁵³ time (months to years) compared to the recurrence time of regular earthquakes
⁵⁴ (up to several hundreds of years), allowing scientists to observe and study many
⁵⁵ complete event cycles, which is typically not possible to explore with traditional
⁵⁶ earthquake catalogs (Beroza and Ide, 2011). A slow slip event on the plate
⁵⁷ boundary is inferred to happen when there is a reversal of the direction of motion
⁵⁸ at GNSS stations, compared to the secular interseismic motion. Slow slip
⁵⁹ events have been observed in many places (Beroza and Ide, 2011; Audet and
⁶⁰ Kim, 2016), such as Cascadia (Bartlow, 2020), Nankai (Nishimura et al., 2013),
⁶¹ Alaska (Li et al., 2016), Costa Rica (Jiang et al., 2012), Mexico (Radiguet
⁶² et al., 2012), and New Zealand (Wallace, 2020).

⁶³

⁶⁴ In many places, tectonic tremor is also observed in relation to slow slip, but
⁶⁵ the spatial **agreement** between tremor and slow slip may vary along the strike
⁶⁶ of the plate boundary (Hall et al., 2018). Tremor is a long (several seconds
⁶⁷ to many minutes), low amplitude seismic signal, with emergent onsets, and an
⁶⁸ absence of clear impulsive phases. Tectonic tremor have been explained as a

69 swarm of small, low-frequency earthquakes (LFEs) (Shelly et al., 2007), which
70 are small magnitude earthquakes ($M \sim 1$) whose frequency content (1-10 Hz) is
71 lower than for ordinary earthquakes (up to 20 Hz). In subduction zones such as
72 Nankai and Cascadia, tectonic tremor observations **agree** spatially and tempo-
73 rally with slow slip observations (Rogers and Dragert, 2003; Obara et al., 2004).
74 Due to this **agreement**, these paired phenomena have been called Episodic
75 Tremor and Slip (ETS). However, this is not always the case. For instance, in
76 northern New Zealand, tremor is more challenging to detect, and seems to be
77 located downdip of the slow slip on the plate boundary (Todd and Schwartz,
78 2016). In Alaska, the tremor zone only partially overlaps the long-term slow
79 slip zone and there does not appear to be any temporal **agreement** between
80 tremor and slow slip occurrence (Wech, 2016).

81
82 In Cascadia, there are robust signals in both slow slip and tremor (Hawthorne
83 and Rubin, 2013). This is also the case in Nankai (Hiramatsu et al., 2008),
84 where tiltmeters are used instead of GNSS. It is thus possible to use tremor as
85 a proxy to observe slow slip events that are not directly observed in the GNSS
86 data. For instance, Aguiar et al. (2009) studied 23 ETS events in Cascadia
87 with more than 50 hours of tectonic tremor. For all these events, they com-
88 puted both the GPS-estimated moment release and the cumulative number of
89 hours of tectonic tremor recorded. They observed a linear relationship between
90 moment release and number of hours of tremor for slow slip events of moment
91 magnitude 6.3 to 6.8. Based on this linear relationship, it is possible to infer
92 the existence of smaller slow slip events of magnitude 5-6 occurring simultane-
93 ously with smaller tremor bursts of duration 1 to 50 hours occurring in between
94 the big ETS events, and for which there is no detectable signal in the GPS data.

95

96 Frank (2016) divided GPS time series observations from Cascadia and Guer-
97 rero, Mexico, into two groups: the first group contains days with abundant
98 tremor and LFEs, the second group contains days when the number of tremor
99 or LFEs is lower than a threshold. He then stacked separately the two groups
100 of daily observations and observed a cumulative displacement in the direction
101 corresponding to the loading period when few tremor or LFEs are observed
102 and the surface deformation corresponds to the secular plate motion. He also
103 observed a cumulative displacement in the opposite direction corresponding to
104 the release period when tremor and LFEs are observed. He was thus able to
105 observe a reverse displacement corresponding to smaller slow slip events not
106 directly observable in the GPS data for individual events.

107

108 However, these methods cannot be applied to detect slow slip events in places
109 where tremor and slow slip occurrence are not well spatially and temporally cor-
110 related, tremor is not abundant, or the seismic network is not robust enough.
111 We thus need other methods to be able to better detect and quantify slow slip.

112

113 Wavelet methods such as the Discrete Wavelet Transform (DWT) are math-
114 ematical tools for analyzing time series simultaneously in the time and the fre-
115 quency domain by observing how weighted differences of a time series vary from
116 one period to the next. Wavelet methods have been widely used for geophysical
117 applications (e.g. Kumar and Foufoula-Georgiou (1997)). However, few studies
118 have used wavelet methods to analyze recordings of slow slip, and their scope
119 was limited to the detection of the bigger (magnitude 6-7) short-term (a few
120 weeks) events (Szeliga et al., 2008; Ohtani et al., 2010; Wei et al., 2012; Alba
121 et al., 2019).

122

123 Szeliga et al. (2008) determined the timing and the amplitude of 34 slow
124 slip events throughout the Cascadia subduction zone between 1997 and 2005
125 using wavelets. They modeled the GPS time series by the sum of a linear trend,
126 annual and biannual sinusoids representing seasonal effects, Heaviside step func-
127 tions corresponding to earthquakes and hardware upgrades, and a residual sig-
128 nal. They then applied a Gaussian wavelet transform to the residual time series
129 to get the exact timing of slow slip at each GPS station. The idea is that the
130 wavelet transform allows us to analyze the signal both in the time and the fre-
131 quency domains. A sharp change in the signal will be localized and seen at all
132 time scales of the wavelet decomposition, contrary to what happens with the
133 periodic sinusoids of the Fourier transform.

134

135 Instead of using wavelets in the time domain, Ohtani et al. (2010) used 2D
136 wavelet functions in the spatial domain to detect slow slip events. They de-
137 signed the Network Stain Filter (NSF) to detect transient deformation signals
138 from large-scale geodetic arrays. They modeled the position of the GPS station
139 by the sum of the secular velocity, a spatially coherent field, site-specific noise,
140 reference frame errors, and observation errors. The spatial displacement field is
141 modeled by the sum of basis wavelets with time-varying weights. Their method
142 has been successfully used to detect a transient event in the Boso peninsula,
143 Japan, and a slow slip event in the Alaska subduction zone (Wei et al., 2012).

144

145 Finally, Alba et al. (2019) used hourly water level records from four tide
146 gauges in the Juan de Fuca Straight and the Puget Sound to determine relative
147 vertical displacements associated with slow slip events between 1996 and 2011.
148 Their main idea is that the tidal level measured at a given gauge is the sum of
149 a noise component at multiple timescales (tides, ocean and atmospheric noise)

150 and an uplift signal due to the slow slip events. The noise component is assumed
151 to be coherent between all tidal gauges, while the tectonic uplift signal is differ-
152 ent provided that the gauges are far enough from each other. By stacking the
153 tidal records after removing tides, the uplift signals cancel each other while the
154 noise signal is amplified. By stacking the components at different time scales of
155 the DWT decomposition, instead of stacking the raw tidal record, each of the
156 components of the noise at different time scales is retrieved and can then be
157 removed from the raw records to obtain the uplift signal. Due to the relative
158 location of the tidal gauges at Port Angeles and Port Townsend compared to the
159 slow slip region on the plate boundary, a slow slip event should result in uplift
160 in Port Angeles (western part) and in subsidence in Port Townsend (eastern
161 part). Indeed, the authors were able to clearly see a difference in the sign of the
162 uplift at these two tidal gauges.

163

164 In our study, we use a similar approach to previous studies with a different
165 reasoning. We only stack signals at nearby GPS stations, assuming that the
166 east-west displacement due to the slow slip events will then be the same at each
167 of the GPS stations considered. We suppose that some of the noise component
168 is different at each GPS station and will be eliminated by the stacking. Finally,
169 we assume that the noise and the longitudinal displacement due to the slow
170 slip events and the secular plate motion have different time scales, so that the
171 wavelet decomposition will act as a bandpass filter to retrieve the displacement
172 signal and highlight the slow slip events. We use wavelet methods to analyze
173 GPS and tremor recordings of slow slip events in Cascadia. Our objective is to
174 verify that there is a good **agreement** between slow slip events detected with
175 only GNSS data, and slow slip events detected with only tremor data. We thus
176 want to demonstrate that the wavelet-based detection method can be applied to

177 detect slow slip events that may currently be obscured using standard methods.
178 Finally, we apply the method to GNSS data in New Zealand and successfully
179 detect several slow slip events without needing to rely on the tremor data.

180

181 2 Data

182 We first focused our study on northwest Washington State. For the GNSS data,
183 we used the GPS time series provided by the Pacific Northwest Geodetic Ar-
184 ray, Central Washington University. These are network solutions in ITRF2014
185 with phase ambiguities resolved with wide-lane phase-biases. Orbit and satel-
186 lite clocks provided by the Jet Propulsion Laboratory/NASA. North, East, and
187 Vertical directions are available. However, as the direction of the secular plate
188 motion is close to the East direction, we only used the East direction of the GPS
189 time series for the data analysis, as it has the best signal-to-noise ratio. The
190 wavelet method works best with data with zero mean, and no sharp discontinu-
191 ities; so we use the cleaned dataset, that is GPS times series with linear trends,
192 steps due to earthquakes or hardware upgrades, and annual and semi-annual
193 sinusoids signals simultaneously estimated and removed following Szeliga et al.
194 (2004). For the tremor data, we used the tremor catalog from the Pacific North-
195 west Seismic Network (PNSN) (Wech, 2010).

196

197 For the application to slow slip events in New Zealand, we used the GPS
198 time series provided by the Geological hazard information for New Zealand
199 (GeoNet). The coordinates have been extracted by GeoNet during the GLOBK
200 run from the combined daily solution files, and converted to (east, north, up)
201 displacement in millimeters with respect to an a priori position and epoch in the
202 ITRF2008 realization. The time series provided by GeoNet have no adjustments

made to them, so they may, for example, contain offsets due to earthquakes, offsets due to equipment changes at individual sites, and seasonal (annual and semi-annual) signals due to various causes. Here again, the direction of the secular interseismic plate motion is close to the West direction, so we only used the East-West component of the GPS time series for the data analysis. We detrended the data before applying the wavelet transform by carrying a linear regression of the whole time series and removing the straight line obtained from the regression.

3 Method

3.1 The Maximal Overlap Discrete Wavelet Transform

The Discrete Wavelet Transform (DWT) is an orthonormal transform that transforms a time series X_t ($t = 0, \dots, N - 1$) into a vector of wavelet coefficients W_i ($i = 0, \dots, N - 1$). If we denote J the level of the wavelet decomposition, and the number of observations is equal to $N = n * 2^J$, where n is some integer greater than or equal to 1, the vector of wavelet coefficients can be decomposed into J wavelet vectors W_j of lengths $\frac{N}{2}, \frac{N}{4}, \dots, \frac{N}{2^J}$, and one scaling vector V_J of length $\frac{N}{2^J}$. Each wavelet vector W_j is associated with changes on time scale $\tau_j = dt2^{j-1}$, where dt is the time step of the time series, and corresponds to the filtering of the original time series with a filter with nominal frequency interval $[\frac{1}{dt2^{j+1}}; \frac{1}{dt2^j}]$. The scaling vector V_J is associated with averages in time scale $\lambda_J = dt2^J$, and corresponds to the filtering of the original time series with a filter with nominal frequency interval $[0; \frac{1}{dt2^{j+1}}]$. Wavelet vectors can be further decomposed into details and smooths, which are more easily interpretable. We define for $j = 1, \dots, J$ the j th wavelet detail D_j , which is a vector of length N , and is associated to time scale $\tau_j = dt2^{j-1}$. Similarly, we can

228 define for $j = 1, \dots, J$ the j th wavelet smooth S_j , which is a vector of length
 229 N , and is associated to scales $\tau_{j+1} = dt2^{j+1}$ and higher. The basic idea is to
 230 reapply to W_j the wavelet filter that was used to construct W_j from the initial
 231 time series X . Together, the details and the smooths define the multiresolution
 232 analysis (MRA) of X :

$$233 \quad X = \sum_{j=1}^J D_j + S_J \quad (1)$$

234 The DWT presents several disadvantages. First, the length of the time se-
 235 ries must be a multiple of 2^J where J is the level of the DWT decompositon.
 236 Second, the time step of the wavelet vector W_j is $dt2^j$, which may not corre-
 237 spond to the time when some interesting phenomenon is visible on the original
 238 time series. Third, when we circularly shift the time series, the corresponding
 239 wavelet coefficients, details and smooths are not a circularly shifted version of
 240 the wavelet coefficients, details and smooths of the original time series. Thus,
 241 the values of the wavelet coefficients, details and smooths are strongly dependent
 242 on the time when we start experimentally gathering the data. Finally, when we
 243 filter the time series to obtain the details D_j and smooths S_j , we introduce a
 244 phase shift, which makes it difficult to line up meaningfully the features of the
 245 MRA with the original time series.

246
 247 To overcome the disadvantages described above, we use instead the Maxi-
 248 mal Overlap Discrete Wavelet Transform (MODWT). The MODWT transforms
 249 the time series X_t ($t = 0, \dots, N - 1$) into J wavelet vectors \tilde{W}_j ($j = 1, \dots, J$) of
 250 length N and a scaling vector \tilde{V}_J of length N . As is the case for the DWT,
 251 each wavelet vector \tilde{W}_j is associated with changes on scale $\tau_j = dt2^{j-1}$, and
 252 corresponds to the filtering of the original time series with a filter with nominal
 253 frequency interval $[\frac{1}{dt2^{j+1}}, \frac{1}{dt2^j}]$. The scaling vector \tilde{V}_J is associated with aver-

254 ages in scale $\lambda_J = dt2^J$, and corresponds to the filtering of the original time
 255 series with a filter with nominal frequency interval $[0; \frac{1}{dt2^{J+1}}]$. As is the case for
 256 the DWT, we can write the MRA:

$$257 \quad X = \sum_{j=1}^J \tilde{D}_j + \tilde{S}_J \quad (2)$$

258 The MODWT of a time series can be defined for any length N . The time
 259 step of the wavelet vectors \tilde{W}_j and the scaling vector \tilde{V}_J is equal to the time
 260 step of the original time series. When we circularly shift the time series, the
 261 corresponding wavelet vectors, scaling vector, details and smooths are shifted
 262 by the same amount. The details and smooths are associated with a zero phase
 263 filter, making it easy to line up meaningfully the features of the MRA with the
 264 original time series. The wavelet methods for time series analysis are explained
 265 in a more detailed way in (Percival and Walden, 2000)).

266

267 **The boundary conditions at the two edges of the time series will**
 268 **affect the wavelet coefficients.** For the MODWT, if we denote L the
 269 length of the base wavelet filter used for the wavelet decomposition
 270 (in our study, we used a Least Asymmetric wavelet filter of length
 271 $L = 8$, see (Percival and Walden, 2000), section 4.8, page 107), the
 272 length of the wavelet filter at level j used to compute the wavelet
 273 detail D_j is:

$$L_j = (2^j - 1)(L - 1) + 1$$

274 The wavelet coefficients of the detail al level j affected by the
 275 boundary conditions at the edges would then be the coefficients with
 276 indices $t = 0, \dots, L_j - 2$ or $t = N - L_j + 1, \dots, N - 1$ (see (Percival

277 and Walden, 2000), section 5.11, page 199). We get $L_j = 442$ for
278 $j = 6$, $L_j = 890$ for $j = 7$ and $L_j = 1786$ for $j = 8$. In practice, the
279 part of the wavelet details affected by the boundary conditions is
280 much shorter than that. We compared the wavelet details computed
281 when using only the data between 2008 and 2012 and the wavelet
282 details computed when using the entire time series from 2000 to 2021
283 (Figure S1 in the Supplementary Material). Even at level 8 only
284 about 6 months of data on each side are effected by the boundary
285 conditions.

286 3.2 Application to synthetic data

287 To illustrate the wavelet transform method, we first apply the MODWT to syn-
288 thetic data. As slow slip events occur in Cascadia on a regular basis, every
289 twelve to eighteen months, we create a synthetic signal of period $T = 500$ days.
290 To reproduce the ground displacement observed on the longitudinal component
291 of GPS stations in Cascadia, we divide each period into two parts: In the first
292 part of duration $T - N$, the displacement is linearly increasing and corresponds
293 to the inter seismic plate motion in the eastern direction; in the second part
294 of duration N , the displacement is linearly decreasing and corresponds to a
295 slow slip event on a reverse fault at depth triggering a ground displacement in
296 the western direction. To see the effect of the duration of the slow slip event,
297 we use different values for $N = 5, 10, 20, 40$ days. The amplitude of the set is
298 normalized to 1. Figure 1 shows the synthetics, the details D_j of the wavelet
299 decomposition for levels 1 to 10, and the smooth S_{10} for the four durations of a
300 slow slip event.

301

302 The ramp-like signal is transformed through the wavelet filtering into a wave-

303 form with first a positive peak and then a negative peak. The shape of the wave-
304 form is the same for every level of the wavelet decomposition, but the width of
305 the waveform increases with the scale level. For the 8th level of the wavelet de-
306 composition, the width of the waveform is nearly as large as the time between
307 two events. At larger scales, the waveforms start to merge two contiguous events
308 together, and make the wavelet decomposition less interpretable. For an event
309 of duration 5 days, the wavelet details at levels higher than 3 have a larger
310 amplitude than the wavelet details at lower scales. For an event of duration 10
311 days, the wavelet details at levels higher than 4 have a larger amplitude than
312 the wavelet details at lower scales. For an event of duration 20 days, the wavelet
313 details at levels higher than 5 have a larger amplitude than the wavelet details
314 at lower scales. For an event of duration 40 days, the wavelet details at levels
315 higher than 6 have a larger amplitude than the wavelet details at lower scales.
316 Thus, the scale levels at which an event is being seen in the wavelet details give
317 us an indication about the duration (and the magnitude) of the slow slip event.
318 The big slow slip events of magnitude 6-7 typically trigger a signal that lasts
319 about one week at an individual GPS station, and the whole event lasts several
320 weeks. We expect them to start being visible at the level 5 of the wavelet de-
321 composition, but to not be noticeable at lower time scales.

322

323 3.3 MODWT of GPS and tremor data

324 The DWT and MODWT methods must be used on a continuous time series,
325 without gaps in the recordings. To deal with the gaps in the GNSS recordings,
326 we simply replace the missing values by interpolation. The value for the first
327 day for which data are missing is equal to the mean of the five days before
328 the gap. The value for the last day for which data are missing is equal to the

mean of the five days after the gap. The remaining missing values are computed by doing a linear interpolation of the first and the last values and adding a Gaussian noise component with mean zero and standard deviation equal to the standard deviation of the whole time series. We verify how the wavelet details may be affected by looking at a GPS time series without missing values and compared the wavelet details with and without removing some data points. Station PGC5 recorded continuous 1390 days between 2009 and 2013 without any missing values. We first computed the wavelet details without missing values. Then, we removed ten neighboring values, replaced them using the method described above (linear interpolation plus Gaussian noise), and computed the wavelet details with the replaced values. Figure S2 in the Supplementary Material shows a comparison of the two wavelet details for two different locations of the missing values. We can see that there are visible differences in the time series itself, and in the details at the smallest levels of the wavelet decomposition. However, the differences between the wavelet details with and without missing values get smaller and smaller with increasing levels of details, and are barely visible for the levels that are most relevant (levels 6 and above). We thus conclude that we can easily replace the missing values in the GNSS time series without introducing false detections of slow slip events.

We then applied the wavelet filtering to real GPS data. Figure 2 shows the longitudinal displacement for GPS station PGC5, located in southern Vancouver Island, the details of the wavelet decomposition for levels 1 to 8, and the smooth. In the data, we can see a sharp drop in displacement whenever there is a documented slow slip event. For levels 5 to 8, which correspond to time scales 16, 32, 64 and 128 days, we can see in the details a positive peak followed by a negative peak whenever there is a drop in displacement in the data. We thus

356 verify that the wavelet method can detect steps in the time series associated
357 with slow slip events.

358

359 To increase the signal-to-noise ratio and better detect slow slip events, we
360 stack the signal from several neighboring GPS stations. We choose to focus on
361 GPS stations located close enough to the tremor zone to get a sufficiently high
362 amplitude of the slow slip signal. We choose 16 points along the 40 km depth
363 contour of the plate boundary (model from Preston et al. (2003)) with spacing
364 equal 0.1 degree in latitude (red triangles on Figure 3). Then we took all the
365 GPS stations located in a 50 km radius for a given point, compute the wavelet
366 details for the longitudinal displacement of each station, and stack each detail
367 over the GPS stations. We thus have a stacked detail for each level 1 to 10 of
368 the wavelet decomposition.

369

370 To assess the success of the wavelet decomposition for detecting slow slip
371 events in GPS time series, we validate the approach by comparing to an inde-
372 pendent proxy for slow slip events. We took all the tremor epicenters located
373 within a 50 km radius centered on one of the 16 locations marked by red trian-
374 gles on Figure 3. Then we computed the cumulative number of tremor within
375 this circle. Finally, we removed a linear trend from the cumulative tremor count,
376 and applied the wavelet transform. Because of the preprocessing applied to the
377 tremor data before that wavelet transform, **the measurement unit associ-**
378 **ated with the corresponding wavelet details is the fraction of tremor**
379 **in a day divided by the total number of days. The average value is**
380 **1 divided by the total number of days.** Figure 4 shows an example of the
381 wavelet decomposition for the third northernmost location on Figure 3 (which
382 is closest to GPS station PGC5). Contrary to what happens for the GPS data,

383 we see a sharp increase in the time series whenever there is a tremor episode,
384 which translates into a negative peak followed by a positive peak in the wavelet
385 details.

386 4 Application to data from Cascadia

387 We stacked the 8th level detail of the wavelet decomposition of the displacement
388 over all the GPS stations located in a 50 km radius of a given point, for the 16
389 locations indicated in Figure 3. The result is shown in the top panel of Figure 5,
390 where each line represents one of the locations along strike. To better highlight
391 the peaks in the wavelet details, we highlighted in red the time intervals where
392 the amplitude of the stacked detail is higher than a threshold, and in blue the
393 time intervals where the amplitude of the stacked detail is lower than minus the
394 threshold. To compare the GPS signal with the tremor signal, we plotted the
395 8th level detail of the wavelet decomposition of the tremor count on the bottom
396 panel of Figure 5. We multiplied by -1 the cumulative tremor count for the
397 wavelet decomposition in order to be able to match positive peaks with positive
398 peaks and negative peaks with negative peaks. In the tremor catalog from the
399 PNSN, there are 17 tremor events with more than 150 hours of tremor recorded.
400 The events are summarized in Table 1. The time of the event is the start date
401 plus half the duration of the event.

402

403 Although the latitudinal extension of the events is not always the same for
404 the GPS data and for the tremor data, we identify the same 13 events in both 8th
405 wavelet decompositions for the 8th level: January 2007, May 2008, May 2009,
406 August 2010, August 2011, September 2012, September 2013, August-November
407 2014, January 2016, March 2017, June 2018, March-November 2019, and Oc-
408 tober 2020-January 2021. Although there are two events in the tremor catalog

409 in August 2014 and November 2014, these two events are not distinguishable in
410 the 8th level details and look more like a single event slowly propagating from
411 South to North. The same phenomenon is observed in 2019 when two tremor
412 events in March and November 2019 are merged into a single event propagating
413 slowly from South to North. In 2020-2021, the wavelet decomposition of the
414 tremor shows one event in the south in October-November 2020 and one event
415 in the North in January 2021, but in the wavelet decomposition of the GPS
416 data, these three events look like a single event propagating slowly from South
417 to North.

418

419 A similar comparison is shown for the wavelet decomposition of the GPS
420 data and the wavelet decomposition of the tremor count data for the 7th level
421 and the 6th level respectively (Figures 6 and 7). The events are harder to see in
422 the 7th level than in the 8th level, both for the GPS data and the tremor count
423 data. The wavelet decomposition is more noisy for the GPS data between 2010
424 and 2012, but it does not seem that there are more slow slip events visible in
425 the 7th level.

426

427 For the 6th level detail, we see an additional event in the South in Fall 2009
428 that is present both in the GPS and the tremor data. It may correspond to the
429 northern extent of a big ETS event occurring in Fall 2009 south of the study
430 area (event 19 in the Michel et al. (2019) catalog). There are three small sig-
431 nals in the GPS data in Winter 2012, Fall 2017, and Winter 2020 that are not
432 present in the tremor data, and may be false detections. To summarize, we
433 assume that robust detections are events present in both GPS and tremor time
434 series, and false detections are events present in the GPS but not in the tremor
435 time series. Then, all the 13 events present on the 8th level detail of the wavelet

436 decomposition are robust detections and 14 of the 17 events present on the 6th
437 level detail of the wavelet decomposition are robust detections.

438

439 To better evaluate the number of robust and false detections, we convert
440 the wavelet details into trinary time series. If the absolute value of the wavelet
441 detail is higher than a threshold, we replace the value by 1 (for positive values)
442 or -1 (for negative values), otherwise we replace the value by 0. We do this
443 on both the wavelet details of the GPS data and of the tremor data. Then we
444 decide that if both the GPS and the tremor time series take the value 1 (or
445 both take the value -1), we have a robust detection (true positive, TP). If the
446 GPS and the tremor time series have opposite signs, or if the absolute value of
447 the GPS time series is 1 but the value of the tremor time series is 0, we have a
448 false detection (false positive, FP). If both time series take the value 0, we do
449 not have detection (true negative, TN). If the GPS time series take the value
450 0, but the absolute value of the tremor time series is 1, we miss a detection
451 (false negative, FN). We then define the sensitivity (true positive rate) and the
452 specificity (equal to 1 minus the false positive rate) as:

$$\begin{aligned} \text{sensitivity} &= \frac{TP}{TP + FN} \\ \text{specificity} &= \frac{TN}{TN + FP} \end{aligned} \quad (3)$$

453 We can then evaluate the quality of the detections obtained with our method
454 by plotting a receiver operating characteristic curve (ROC curve). The ROC
455 curve is widely used for binary classification problems in statistics and machine
456 learning. We calculate an ROC value by varying the values of the threshold
457 (here the two thresholds used to convert the GPS and the tremor time series
458 into trinary time series), computing the corresponding values of the true positive
459 rate and the false positive rate (equal to 1 minus the specificity), and plotting

460 the true positive rate as a function of the false positive rate. If the classifica-
461 tion was made randomly, all the points would fall on the first diagonal. If the
462 classifier was perfect, the corresponding point would fall on the top left cor-
463 ner of the graph with true positive rate equal to 1 and false positive rate equal
464 to 0. The bigger the area under the curve, the better the classification method is.

465

466 As the slow slip events are better seen on levels 6, 7 and 8 of the wavelet
467 decomposition, we first add the wavelet details corresponding to levels 6 to 8,
468 and transform the resulting time series into a trinary time series. We apply this
469 transform to both the GPS and the tremor time series with varying thresholds.
470 We then plot the ROC curve on Figure 8, each dot representing a different
471 threshold. The corresponding sums of the wavelet details for the GPS data and
472 the tremor data are shown on Figure 9. We can see that there is a trade-off
473 between sensitivity and specificity as we vary the threshold. If we decrease the
474 false positive rate, we also decrease the number of true events detected. If we
475 increase the number of true events detected, we also increase the false positive
476 rate. If we increase the threshold for the tremor, the curve goes farther away
477 from the first diagonal, that is we get better classification results. If we increase
478 the threshold for the GPS, the false positive rate and the the number of events
479 detected decrease. In Figure 9, we have chosen thresholds for the GPS time
480 series and the tremor time series such that the specificity is higher than 0.75
481 (that is the false positive rate is lower than 0.25), and the sensitivity is the
482 highest possible, that is we have chosen the thresholds corresponding to the dot
483 that is farthest from the diagonal, which is random.

484

485 In addition to the magnitude 6 events discussed above, Michel et al. (2019)
486 have also identified several magnitude 5 events using a variational Bayesian In-

487 dependent Component Analysis (vbICA) decomposition of the signal. As we
488 expect smaller magnitude events to be more visible at smaller time scales of the
489 wavelet decomposition (level 5), we verify for all these events whether a signal
490 can be seen at the same time as the time given in their catalog. Most of these
491 magnitude 5 events are also sub-events of bigger magnitude 6 events. Table
492 2 summarizes for each event its timing, its number and its magnitude as indi-
493 cated in the catalog from Michel et al. (2019), and whether it is part of a bigger
494 magnitude 6 event. Figure 10 shows the 5th level detail wavelet decomposition
495 of the GPS data. Red lines show the timing of the big slow slip events from
496 Table 1, and blue lines show the timing of the small slow slip events from Table 2.

497

498 All 14 events that are sub-events of a bigger event are visible at level 5.
499 However, this may be because the bigger events are clearly seen at levels 6 to 8,
500 and also at smaller time scales. The one small event that is not part of a bigger
501 event (Winter 2009) is visible at level 5 of the wavelet decomposition. However,
502 some other events that are not in the catalog of Michel et al. (2019)'s catalog
503 are also visible in late 2007, early 2010, early 2012, and early 2020. Therefore,
504 it is difficult to differentiate between a robust detection and a false detection,
505 and to conclude whether the method can indeed detect events of magnitude 5.

506

507 In Figure 9, we see four smaller events that are not in the catalog of Michel
508 et al. (2019): at about 2007.5, there is a negative peak followed by a positive
509 peak (that is an event in the opposite direction of what would be expected from
510 slow slip), at about 2010.2, 2012.2 and 2020.2, there are positive peaks followed
511 by negative peaks for all the sixteen locations studied in this paper. These
512 events are highlighted in Figure S4 in the Supplementary Information. Looking
513 back at the original GPS data, there is a small increase in the displacement

514 in the eastern direction that lasts about one or two months at about 2007.5.
515 However, the direction of the displacement does not correspond to a slow slip
516 event, and another cause should be found to explain this signal. There is a de-
517 crease in displacement that lasts several months at about 2010.2. This transient
518 may correspond to a long duration slow slip event. There is a small decrease
519 in displacement at about 2012.2. Its amplitude is small but the duration and
520 direction correspond to a slow slip event, so this transient could be a very small
521 slow slip event. Finally, there is also a small decrease in displacement at about
522 2020.2 that is difficult to interpret.

523

524 Due to the short distances between the GPS stations and the locations of the
525 red triangles on the map from Figure 3, the same station could be used multiple
526 times for the stacking at different locations. When considering two different lo-
527 cations, the stacking is thus made over an overlapping number of stations. Table
528 3 summarizes the number of stations and the number of overlapping stations for
529 each location on Figure 3. We hypothesize that the small displacement in the
530 eastern direction seen at about 2007.5 could be due to a misbehaving station
531 common to several locations. However, several GPS stations indeed show an
532 increase in the displacement in the eastern direction at about 2007.5. There are
533 many missing data around that time, so it is difficult to conclude.

534

535 Another possibility is that common mode signals could stack constructively
536 across GNSS stations and produce peaks in the wavelet details that are actually
537 due to non-tectonic signals. We computed common mode signals for different
538 latitude bins (each bin has width equal to half-a-degree of latitude) following
539 the same method as Nuyen and Schmidt (2021). We first stacked all the time
540 series for the stations in each latitude bin that are located more than 100 km

541 east of the 40 km depth contour of the plate boundary. We assume that these
542 stations are not sensitive to the deformation on the plate interface. We then
543 apply a yearly moving average to each common mode signal in order to remove
544 any leftover noise. The common mode signal was then removed from the GNSS
545 time series depending on each sites latitude. Figure S3 in the Supplementary
546 Information shows the corresponding sum of the stacks of the 6th, 7th and 8th
547 wavelet details obtained from the resulting time series. The common modes
548 seem to have little impact on the results and do not explain the additional four
549 small events that we noted in Figure 9.

550

551 In order to convert our filtered eastward displacement time series into a slow
552 slip event catalog we note that red bars represent displacements exceeding a
553 threshold of 0.8 mm (east), and blue marks displacements less than minus -0.8
554 mm (west). During times with no slow slip GPS stations on the overriding plate
555 are pushed slowly eastward by the locked subducting plate. Slow slip events
556 represent GPS motion **towards** the west. Thus, we infer that slow slip events
557 happen when red bars are immediately followed by blue bars in the wavelet
558 details. We have identified everywhere that this has happened and mark it with
559 a green line in Figure 11 and as a row in Table 4. We find 17 possible SSEs
560 by this method using filtered GPS data only. For each of these 17 events we
561 determine the time difference between the mid time of the GPS catalog and the
562 nearest time from the tremor catalog (Table 1). These time differences are in
563 column 6 (Table 4). Every event in the GPS catalog has a match in the tremor
564 catalog except for the tremor event at 2010.15. There is also only one event in
565 the tremor catalog that is not in the GPS catalog. It occurs at 2014.65 with
566 a duration of 15 days and 190 hours of tremor. It occurs 0.25 years after the
567 nearest GPS event. There are also two marginal events in the tremor catalog

568 with time differences of 0.13 and 0.10 years, but those are also among the smaller
569 events with 162 and 193 hours of tremor.

570 5 Application to data from New Zealand

571 We now apply our wavelet-based method to detect slow slip events in New
572 Zealand, a location where **the spatial and temporal agreement between**
573 **tremor and slow slip is not as good as in** other subduction zones. The
574 tectonics of the North Island of New Zealand are dominated by the westward
575 subduction of the Pacific Plate under the Australian Plate at the Hikurangi
576 Trench. Two types of slow slip events have been observed at the Hikurangi
577 margin. Shallow (10-15 km depth), shorter (1-3 weeks), and usually smaller
578 (Mw 6.3-6.8) slow slip events have been observed every 18-24 months in the
579 northern part of the margin. Deeper (35-60 km depth), longer (12-18 months),
580 and larger (Mw 7.0) slow slip events have been observed every 5 years in the
581 southern part of the margin (Wallace and Beavan, 2010; Todd and Schwartz,
582 2016). The detection of tremor has been elusive in northern Hikurangi. Dela-
583 haye et al. (2009) observed an increase in the rate of microseismicity downdip of
584 the 2004 Gisborne slow slip event. More recently, however, (Kim et al., 2011)
585 detected a low level of tremor activity that increased during the 2010 Gisborne
586 slow slip event. As was the case for the microearthquakes, the source of the
587 tremor was located downdip of the slow slip patch determined from GNSS data.
588 (Ide, 2012) detected tremor downdip of the location of two deep slow slip events
589 observed by Wallace and Eberhart-Phillips (2013) in 2006 and 2008. However,
590 contrary to ETS events in Cascadia and Nankai, the tremor activity did not
591 seem to increase during the slow slip events. Todd and Schwartz (2016) de-
592 tected tremor associated with most of the shallow slow slip events between 2010
593 and 2015, and located downdip of the geodetically inferred slip area. They also

594 detected deeper tremor between 20 and 50 km depth with unclear origin. They
595 hypothesized that these tremor may be related to undetected deep long-term
596 slow slip events.

597

598 To evaluate whether the wavelet analysis is effective in a region without
599 robust tremor, we take all the New Zealand GPS stations located in a 50 km
600 radius of a given **location**, for the 18 locations indicated in Figure 12, and we
601 stack the 6th level details, the 7th level details or the 8th level details over all
602 the GPS stations. We then sum together the 6th, 7th and 8th levels stacked
603 wavelet details (Figure 13, top panel). We highlight positive and negative peaks
604 with red and blue colors as was done in Figure 9. We cannot use the tremor data
605 to decide what is the appropriate threshold above which we consider that there
606 is a slow slip event. **Slow slip events in New Zealand result in surface**
607 **displacements that are similar in amplitude to twice as large as those**
608 **observed in Cascadia.** Therefore, the amplitudes of the peaks in the wavelet
609 details should be similar in New Zealand and in Cascadia and we choose iden-
610 tical thresholds for both regions. As a slow slip event in northern New Zealand
611 results in a displacement in the east direction at the earths surface, the slow
612 slip events are indicated by a negative peak followed by a positive peak in the
613 stacked wavelet details. We compare the results of the timings and locations
614 of the slow slip events to those events detected by Todd and Schwartz (2016).
615 As they only used data from five GPS stations (PUKE, ANAU, GISB, MAHI
616 and CKID), we indicate by a vertical orange bar on the bottom panel of Figure
617 13 each time a slow slip event was detected for these stations. The orange bars
618 are centered on the latitudes of the GPS stations. If a slow slip event was de-
619 tected by more than one station, all the corresponding orange bars are linked
620 together to show the spatial extent of the slow slip. Todd and Schwartz (2016)

621 indicated by a question mark (on their Figure 2 and their Table 1) additional
622 possible events, and those are indicated by a dotted orange bar on Figure 13.
623 To compare with the slow slip events detected with the wavelet method, we also
624 mark by a green bar every time a negative peak lower than the threshold is
625 followed by a positive peak higher than the threshold. Table 5 summarizes the
626 slow slip events detected with the wavelet method for 2010-2016.

627

628 We observe that there is a good **agreement** between the events detected
629 with the wavelet method and the events previously detected by Todd and
630 Schwartz (2016). We clearly see an event propagating from south to north
631 in January-February (event 2 from Todd and Schwartz (2016)), an event in
632 March-April 2010 (event 3), an event in April-May 2011 in the northern part
633 of the region studied (events 6 and 7), an event propagating south-to-north in
634 August-September and September-October 2011 (events 8 and 9), and an event
635 in December 2011 (event 10). Although Todd and Schwartz (2016) only de-
636 tected this last event for GPS station GISB, it seems that this event may have
637 also extended farther to the north and the south. We then clearly see an event
638 in the northern part of the region studied in August 2012 (event 12), an event
639 in December 2012-January 2013 (event 13), an event in the southern part of
640 the region studied in February-March 2013 (event 14), an event propagating
641 from south to north in June-July and July-August 2013 (events 15 and 16), an
642 event in September 2014 (events 20 and 21), an event in the southern part of
643 the region studied in December 2014-January 2015 (events 22 and 23), and an
644 event in June-July 2015 in the northern part of the region studied (event 26).
645 It is unclear if the event near station ANAU in early 2010 (event 1) is visible
646 in the wavelet details as it is too close to the beginning of the time series. The
647 June-July 2010 event (event 4), the August 2010 event (event 5), and the March

648 2012 event (event 11), are not clearly visible in the wavelet details. The events
649 in September-October 2013 (event 17), December 2013 (event 18), May-June
650 2014 (event 19), January-February (event 24) and February 2015 (events 25)
651 are not clearly seen in the wavelet details, but there could be a small negative
652 peak followed by a small positive peak at these times. Additionally, there could
653 be two other events that are not in (Todd and Schwartz, 2016) in Fall 2010
654 (southern part of the region studied) and in Fall 2015.

655

656 Our wavelet-based method thus works well to detect transients in GPS data
657 that could be slow slip events, even in the absence of tremor data. The choice
658 of the appropriate threshold to decide that there is a transient and the levels
659 of the wavelet details that we look at for the detection may still not be easily
660 made. There is a difference between Cascadia and New Zealand in terms of
661 which wavelet details to stack. In particular, as there is more time between
662 two slow slip events in New Zealand than in Cascadia, the biggest slow slip
663 events (early 2010, late 2011, 2013 and late 2014) can also be **seen** on the 9th
664 level detail for New Zealand, whereas they could not be seen for Cascadia. We
665 then use the method to detect slow slip events during the period 2016-2022,
666 which was not covered by Todd and Schwartz (2016) (Figure 14). We note
667 four large transients that could be slow slip events in late 2016, late 2017, early
668 2019 and mid-2021. There are also possible smaller events in the northern part
669 of the area in mid-2018 and in most of the area studied in early 2020. Table 6
670 summarizes the slow slip events detected with the wavelet method for 2016-2022.

671

672 **The method is thus applicable in regions where tremor data are**
673 **not usable. To determine which wavelet levels to stack, we recom-**
674 **mend analyzing each level detail. Look for spatially coherent pat-**

675 terms, wavelet details with energy at similar times and high signal-
676 to-noise ratios. Look for alternating positive and negative peaks that
677 are consistent with the expected direction of slow slip. Consider
678 wavelet details with time scales ranging from the expected duration
679 of slow slip events to the expected recurrence times between slow slip
680 events. For Cascadia and New Zealand this would be weeks to years.
681 Determination of a threshold is subjective. At large thresholds the
682 large slow slip events should be clear. At smaller thresholds there is
683 the possibility of identifying smaller events, but at the risk of false
684 detections.

685 6 Conclusion

686 In this paper, we develop and test a new approach for detecting transient events
687 in GPS time series, such as slow slip events. We used wavelet methods to analyze
688 GNSS time series and tremor recordings of slow slip events in Cascadia, and
689 GNSS time series in New Zealand. We used detrended GNSS data, applied the
690 MODWT transform, and stacked the wavelet details over several nearby GNSS
691 stations. As an independent check on the timing of slow slip events, we also
692 computed the cumulative number of tremor in the vicinity of the GNSS stations,
693 detrended this signal, and applied the MODWT transform. In both time series,
694 we could then see simultaneous waveforms whose timing corresponds to the
695 timing of slow slip events. We assumed that there is a slow slip event whenever
696 the wavelet signal gets above a threshold. We verified that there is a good
697 **agreement** between slow slip events detected with only GNSS data, and slow
698 slip events detected with only tremor data. The wavelet-based detection method
699 detects all events of magnitude higher than 6 as determined by independent
700 event catalogs (e.g. (Michel et al., 2019)). We detected signals in the GPS data

701 that could be magnitude 5 events, but it is not easy to differentiate between
702 robust detections and false detections. We then applied the method to GNSS
703 data in New Zealand and detected slow slip events consistent with the events
704 previously detected by Todd and Schwartz (2016).

705 Data and Resources

706 The GPS recordings used for this analysis can be downloaded from the PANGA
707 website (GPS/GNSS Network and Geodesy Laboratory: Central Washington
708 University, other/seismic network, 1996) <http://www.panga.cwu.edu/> and the
709 Geonet website <https://www.geonet.org.nz/>. The Python scripts used to
710 analyze the data and make the figures can be found on the first author's Github
711 account <https://github.com/ArianeDucellier/slowslip>. Figures 3 and 12
712 were created using GMT (Wessel and Smith, 1991). **The Supplementary**
713 **Material contains three figures showing the effects of boundary con-**
714 **ditions, missing data and common modes, and a figure showing four**
715 **additional small displacements detected in the GPS data.**

716 Acknowledgements

717 The authors would like to thank two anonymous reviewers and the Associate Ed-
718 itor Jeanne Hardebeck, whose comments greatly helped improve the manuscript.
719 This work was funded by the grant from the National Science Foundation EAR-
720 1358512. A.D. would like to thank Professor Donald Percival for introducing
721 her to wavelet methods during his excellent class on Wavelets: Data Analysis,
722 Algorithms and Theory taught at University of Washington.

⁷²³ **Declaration of Competing Interests**

⁷²⁴ The authors declare no competing interests.

⁷²⁵ **References**

- ⁷²⁶ Aguiar, A., Melbourne, T., and Scrivner, C. Moment release rate of Cascadia
⁷²⁷ tremor constrained by GPS. *J. Geophys. Res.*, 114:B00A05, 2009.
- ⁷²⁸ Alba, S., Weldon, R. J., Livelybrooks, D., and Schmidt, D. A. Cascadia ETS
⁷²⁹ events seen in tidal records (1980–2011). *Bull. Seismol. Soc. Am.*, 109(2):
⁷³⁰ 812–821, 2019.
- ⁷³¹ Audet, P. and Kim, Y. Teleseismic constraints on the geological environment
⁷³² of deep episodic slow earthquakes in subduction zone forearcs: A review.
⁷³³ *Tectonophysics*, 670:1–15, 2016.
- ⁷³⁴ Bartlow, N. M. A longterm view of episodic tremor and slip in Cascadia. *Geo-
physical Research Letters*, 43(3):e2019GL085303, 2020.
- ⁷³⁶ Beroza, G. and Ide, S. Slow earthquakes and nonvolcanic tremor. *Annu. Rev.
Earth Planet. Sci.*, 39:271–296, 2011.
- ⁷³⁸ Delahaye, E., Townend, J., Reyners, M., and Rogers, G. Microseismicity but
⁷³⁹ no tremor accompanying slow slip in the Hikurangi subduction zone, New
⁷⁴⁰ Zealand. *Earth and Planetary Science Letters*, 277:21–28, 2009.
- ⁷⁴¹ Frank, W. Slow slip hidden in the noise: The intermittence of tectonic release.
⁷⁴² *Geophys. Res. Lett.*, 43:10125–10133, 2016.
- ⁷⁴³ GPS/GNSS Network and Geodesy Laboratory: Central Washington University,
⁷⁴⁴ other/seismic network. Pacific Northwest Geodetic Array (PANGA), 1996.
⁷⁴⁵ URL <http://www.panga.cwu.edu/>.

- 746 Hall, K., Houston, H., and Schmidt, D. Spatial comparisons of tremor and slow
747 slip as a constraint on fault strength in the northern Cascadia subduction
748 zone. *Geochemistry, Geophysics, Geosystems*, 19(8):2706–2718, 2018.
- 749 Hawthorne, J. C. and Rubin, A. M. Shorttime scale correlation between slow
750 slip and tremor in Cascadia. *Journal of Geophysical Research: Solid Earth*,
751 118:1316–1329, 2013.
- 752 Hiramatsu, Y., Watanabe, T., and Obara, K. Deep lowfrequency tremors as a
753 proxy for slip monitoring at plate interface. *Geophysical Research Letters*, 35:
754 L13304, 2008.
- 755 Ide, S. Variety and spatial heterogeneity of tectonic tremor worldwide. *Journal*
756 *of Geophysical Research*, 117:B03302, 2012.
- 757 Jiang, Y., Wdowinski, S., Dixon, T. H., Hackl, M., Protti, M., and Gonzalez,
758 V. Slow slip events in Costa Rica detected by continuous GPS observations,
759 2002-2011. *Geochemistry, Geophysics, Geosystems*, 13:Q04006, 2012.
- 760 Kim, M., Schwartz, S., and Bannister, S. Nonvolcanic tremor associated with
761 the March 2010 Gisborne slow slip event at the Hikurangi subduction margin,
762 New Zealand. *Geophysical Research Letters*, 38:L14301, 2011.
- 763 Kumar, P. and Foufoula-Georgiou, E. Wavelet analysis for geophysical applica-
764 tions. *Rev. Geophys.*, 35(4):385–412, 1997.
- 765 Li, S., Freymueller, J., and McCaffrey, R. Slow slip events and timedependent
766 variations in locking beneath Lower Cook Inlet of the AlaskaAleutian sub-
767 duction zone. *Journal of Geophysical Research: Solid Earth*, 121:1060–1079,
768 2016.
- 769 Michel, S., Gualandi, A., and Avouac, J.-P. Interseismic coupling and slow slip

- 770 events on the Cascadia megathrust. *Pure Appl. Geophys.*, 176:3867–3891,
771 2019.
- 772 Nishimura, T., Matsuzawa, T., and Obara, K. Detection of shortterm slow slip
773 events along the Nankai Trough, southwest Japan, using GNSS data. *Journal*
774 *of Geophysical Research: Solid Earth*, 118:3112–3125, 2013.
- 775 Nuyen, C. P. and Schmidt, D. A. Filling the gap in Cascadia: The emergence
776 of lowamplitude longterm slow slip. *Geochemistry, Geophysics, Geosystems*,
777 22(3):e2020GC009477, 2021.
- 778 Obara, K., Hirose, H., Yamamizu, F., and Kasahara, K. Episodic slow slip
779 events accompanied by non-volcanic tremors in southwest Japan subduction
780 zone. *Geophysical Research Letters*, 31:L23602, 2004.
- 781 Ohtani, R., McGuire, J., and Segall, P. Network strain filter: A new tool for
782 monitoring and detecting transient deformation signals in GPS arrays. *J.*
783 *Geophys. Res.*, 115:B12418, 2010.
- 784 Percival, D. and Walden, A. *Wavelet Methods for Time Series Analysis*. Cam-
785 bridge Series in Statistical and Probabilistic Mathematics. Cambridge Uni-
786 versity Press, New York, NY, USA, 2000.
- 787 Preston, L., Creager, K., Crosson, R., Brocher, T., and Trehu, A. Intraslab
788 earthquakes: Dehydration of the Cascadia slab. *Science*, 302:1197–1200, 2003.
- 789 Radiguet, M., Cotton, F., Vergnolle, M., Campillo, M., Walpersdorf, A., Cotte,
790 N., and Kostoglodov, V. Slow slip events and strain accumulation in the
791 Guerrero gap, Mexico. *Journal of Geophysical Research: Solid Earth*, 117:
792 B04305, 2012.
- 793 Rogers, G. and Dragert, H. Tremor and slip on the Cascadia subduction zone:
794 The chatter of silent slip. *Science*, 300(5627):1942–1943, 2003.

- 795 Schmidt, D. A. and Gao, H. Source parameters and timedepependent slip dis-
796 tributions of slow slip events on the Cascadia subduction zone from 1998 to
797 2008. *Journal of Geophysical Research: Solid Earth*, 115:B00A18, 2010.
- 798 Shelly, D., Beroza, G., and Ide, S. Non-volcanic tremor and low-frequency
799 earthquake swarms. *Nature*, 446:305–307, 2007.
- 800 Szeliga, W., Melbourne, T., Miller, M., and Santillan, V. Southern Cascadia
801 episodic slow earthquakes. *Geophys. Res. Lett.*, 31:L16602, 2004.
- 802 Szeliga, W., Melbourne, T., Santillan, M., and Miller, M. GPS constraints on 34
803 slow slip events within the Cascadia subduction zone, 1997-2005. *J. Geophys.*
804 *Res.*, 113:B04404, 2008.
- 805 Todd, E. and Schwartz, S. Tectonic tremor along the northern Hikurangi Mar-
806 gin, New Zealand, between 2010 and 2015. *J. Geophys. Res. Solid Earth*, 121:
807 8706–8719, 2016.
- 808 Vergnolle, M., Walpersdorf, A., Kostoglodov, V., Tregoning, P., Santiago, J. A.,
809 Cotte, N., and Franco, S. I. Slow slip events in Mexico revised from the
810 processing of 11 year GPS observations. *Journal of Geophysical Research:*
811 *Solid Earth*, 115:B08403, 2010.
- 812 Wallace, L. M. Slow slip events in New Zealand. *Annual Review of Earth and*
813 *Planetary Sciences*, 48:175–203, 2020.
- 814 Wallace, L. M., Beavan, J., Bannister, S., and Williams, C. Simultaneous
815 longterm and shortterm slow slip events at the Hikurangi subduction margin,
816 New Zealand: Implications for processes that control slow slip event occur-
817 rence, duration, and migration. *Journal of Geophysical Research: Solid Earth*,
818 117:B11402, 2012.

- 819 Wallace, L. and Beavan, J. Diverse slow slip behavior at the Hikurangi sub-
820 duction margin, New Zealand. *Journal of Geophysical Research*, 115:B12402,
821 2010.
- 822 Wallace, L. and Eberhart-Phillips, D. Newly observed, deep slow slip events at
823 the central Hikurangi margin, New Zealand: Implications for downdip vari-
824 ability of slow slip and tremor, and relationship to seismic structure. *Geo-
825 physical Research Letters*, 40:5393–5398, 2013.
- 826 Wech, A. Interactive tremor monitoring. *Seismol. Res. Lett.*, 81(4):664–669,
827 2010.
- 828 Wech, A. Extending Alaska’s plate boundary; tectonic tremor generated by
829 Yakutat subduction. *Geology*, 44(7):587–590, 2016.
- 830 Wei, M., McGuire, J., and Richardson, E. A slow slip event in the south central
831 Alaska Subduction Zone. *Geophys. Res. Lett.*, 39:L15309, 2012.
- 832 Wessel, P. and Smith, W. H. F. Free software helps map and display data. *EOS
833 Trans. AGU*, 72:441, 1991.
- 834 Williams, C. A., Eberhart-Phillips, D., Bannister, S., Barker, D. H., Henrys, S.,
835 Reyners, M., and Sutherland, R. Revised interface geometry for the Hikurangi
836 subduction zone, New Zealand. *Seismological Research Letters*, 84(6):1066–
837 1073, 2013.

⁸³⁸ **Addresses**

⁸³⁹ Ariane Ducellier. University of Washington, Department of Earth and Space
⁸⁴⁰ Sciences, Box 351310, 4000 15th Avenue NE Seattle, WA 98195-1310.

⁸⁴¹

⁸⁴² Kenneth C. Creager. University of Washington, Department of Earth and
⁸⁴³ Space Sciences, Box 351310, 4000 15th Avenue NE Seattle, WA 98195-1310.

⁸⁴⁴

⁸⁴⁵ David A. Schmidt. University of Washington, Department of Earth and
⁸⁴⁶ Space Sciences, Box 351310, 4000 15th Avenue NE Seattle, WA 98195-1310.

Tables

Table 1: Episodic Tremor and Slip events with $M > 6$ identified by MODWT in both the GPS and the tremor data. The duration and the number of tremor are from the tremor catalog of the PNSN. The event number and the magnitude are from the slow slip catalog of Michel et al. (2019).

Time	Duration (days)	Number of tremor (hours)	Event number	Magnitude
2007.06	28	398	3	6.68
2008.36	25	402	10	6.56
2009.35	24	248	16	6.49
2010.63	29	518	24	6.54
2011.60	37	479	30	6.47
2012.72	37	620	34	6.54
2013.71	27	423	41	6.58
2014.65	15	190	48	6.03
2014.89	38	385	51	6.40
2016.11	43	421	54	6.79
2017.23	19	279	59	6.61
2018.49	22	381		
2019.23	34	195		
2019.88	16	205		
2020.79	26	193		
2020.86	12	162		
2021.09	14	230		

Table 2: Magnitude **5 to 6** events from Michel et al. (2019).

Time	Event number	Magnitude	Sub-event of bigger event
2007.06	1	5.64	Yes
2007.08	2	5.91	Yes
2008.38	11	5.50	Yes
2009.16	14	5.50	No
2009.36	17	5.32	Yes
2010.63	25	5.76	Yes
2011.66	31	5.61	Yes
2011.66	32	5.32	Yes
2012.69	35	5.56	Yes
2013.74	42	5.71	Yes
2014.69	49	5.31	Yes
2014.93	52	5.39	Yes
2016.03	57	5.80	Yes
2017.13	60	5.43	Yes
2017.22	61	5.37	Yes

Table 3: Number of GPS stations used for the stacking for each location on Figure 3 and number of common stations with the location immediately to the north and the location immediately to the south.

Index	Latitude	Number of stations	Common stations (north)	Common stations (south)
0	47.2	15	14	
1	47.3	18	17	14
2	47.4	24	20	17
3	47.5	21	20	20
4	47.6	22	14	20
5	47.7	17	12	14
6	47.8	13	8	12
7	47.9	10	9	8
8	48.0	10	7	9
9	48.1	8	7	7
10	48.2	10	8	7
11	48.3	9	9	8
12	48.4	9	5	9
13	48.5	7	5	5
14	48.6	6	5	5
15	48.7	5		5

Table 4: Cascadia catalog of slow slip events based only on MODWT analysis of GPS time series and inferring that the transition of red followed immediate by blue marks a slow slip event. First four columns are the start and end times and start and end latitudes of the green bars in Figure 11. The fifth column is 1 for robust detection and 2 if not as robust. Column 6 is the time difference in years between the mid times of the GPS catalog and the nearest mid times of the tremor catalog summarized in Table 1.

start time	end time	start latitude	end latitude	dT	tremor catalog
2007.06	2007.10	47.16	48.72	1	0.02
2008.30	2008.40	47.35	48.73	1	0.01
2009.35	2009.44	47.92	48.73	1	0.05
2010.12	2010.15	47.32	48.73	1	0.50 no match
2010.61	2010.64	47.17	48.72	1	0.00
2011.57	2011.61	47.18	48.68	1	0.01
2012.65	2012.65	48.74	47.76	1	0.05
2013.71	2013.75	47.47	48.73	1	0.02
2014.89	2014.90	48.73	47.79	1	0.01
2015.98	2016.09	48.73	47.20	1	0.08
2017.17	2017.24	47.38	48.72	1	0.02
2018.35	2018.36	47.48	47.93	1	0.13 part of same event?
2018.48	2018.50	48.72	48.09	1	0.00
2019.32	2019.34	47.17	47.72	2	0.10
2019.90	2019.91	48.47	48.72	2	0.02
2020.79	2020.83	47.18	48.13	1	0.02 & 0.05
2021.11	2021.12	48.75	48.48	2	0.02

Table 5: New Zealand catalog of slow slip events for 2010-2016 based only on MODWT analysis of GPS time series and inferring that the transition of red followed immediate by blue marks a slow slip event. First four columns are the start and end times and start and end latitudes of the green bars in Figure 13. The fifth column is 1 for robust detection and 2 if not as robust.

start time	end time	start latitude	end latitude	
2010.05	2010.07	-39.67	-39.12	1
2010.19	2010.22	-39.12	-38.07	1
2010.75	2010.76	-39.73	-39.41	1
2011.36	2011.37	-38.22	-38.02	2
2011.71	2011.74	-37.97	-38.41	1
2011.67	2011.71	-39.73	-38.91	1
2011.92	2011.95	-38.84	-38.16	1
2012.63	2012.63	-39.42	-39.62	2
2012.64	2012.66	-38.53	-38.02	1
2012.95	2012.96	-38.32	-37.98	1
2013.15	2013.16	-38.87	-39.72	1
2013.55	2013.57	-38.62	-38.01	1
2013.74	2013.74	-38.77	-38.97	2
2013.92	2013.93	-38.17	-37.98	2
2013.91	2013.95	-39.37	-39.73	1
2014.78	2014.79	-38.03	-39.03	1
2014.96	2015.00	-39.07	-39.72	1
2015.53	2015.53	-39.42	-39.72	1
2015.52	2015.55	-37.97	-38.43	1
2015.78	2015.79	-38.77	-39.37	1

Table 6: New Zealand catalog of slow slip events for 2016-2022 based only on MODWT analysis of GPS time series and inferring that the transition of red followed immediate by blue marks a slow slip event. First four columns are the start and end times and start and end latitudes of the green bars in Figure 13. The fifth column is 1 for robust detection and 2 if not as robust.

start time	end time	start latitude	end latitude	
2016.84	2016.90	-37.96	-39.72	1
2017.10	2017.10	-38.78	-39.00	2
2017.73	2017.78	-37.98	-38.51	1
2018.04	2018.06	-38.58	-39.07	1
2018.63	2018.64	-38.27	-37.97	2
2019.26	2019.33	-37.97	-39.73	1
2020.09	2020.12	-37.97	-38.23	2
2020.34	2020.35	-37.96	-39.72	1
2020.33	2020.33	-37.96	-38.10	2
2020.32	2020.32	-38.62	-38.79	2
2020.36	2020.37	-39.70	-39.35	2
2021.11	2021.11	-39.51	-39.64	2
2021.39	2021.47	-39.72	-38.08	1

848 **Figure captions**

- 849 • Figure 1. Demonstration of a wavelet decomposition for a synthetic dataset.
850 A synthetic time series is created (top row) with steps of period 500 days,
851 and transient durations of 2 days (left), 5 days, 10 days, and 20 days
852 (right). The resulting details and smooths are shown in increasing level.
853 The amplitude of the synthetic time series is normalized to 1, and the
854 details and smooths show the relative amplitude.
- 855 • Figure 2. Top left: **East-west** displacement recorded at GPS station
856 PGC5. The resulting details and smooth of the wavelet decomposition
857 are shown in increasing level from top to bottom and from left to right.
- 858 • Figure 3. GPS stations used in this study (black triangles). The black
859 line represents the 40 km depth contour of the plate boundary model by
860 Preston et al. (2003). The red triangles are the locations where we stack
861 the GPS data. The small grey dots are all the tremor locations from the
862 PNSN catalog.
- 863 • Figure 4. Details and smooth of the wavelet decomposition of the de-
864 trended cumulative tremor count around the third northernmost red tri-
865 angles on Figure 3 (latitude 48.5).
- 866 • Figure 5. Top: Stacked 8th level details of the wavelet decomposition of
867 the displacement over all the GPS stations located in a 50 km radius of a
868 given point, for the 16 red triangles indicated in Figure 3. Bottom: 8th
869 level detail multiplied by -1 of the cumulative tremor count in a 50 km
870 radius of a given point for the same 16 locations. The black lines represent
871 the timings of the ETS events from Table 1. We mark by a red rectangle
872 every time where the amplitude is higher than a threshold of 0.4 mm (for
873 the GPS) or 0.003 (for the tremor, **that is about 17 times the average**

874 **value of the signal)**. We mark by a blue rectangle every time where the
875 amplitude is lower than minus the threshold.

876 ● Figure 6. Top: Stacked 7th level details of the wavelet decomposition of
877 the displacement over all the GPS stations located in a 50 km radius of a
878 given point, for the 16 red triangles indicated in Figure 3. Bottom: 7th
879 level detail multiplied by -1 of the cumulative tremor count in a 50 km
880 radius of a given point for the same 16 locations. The black lines represent
881 the timings of the ETS events from Table 1. We mark by a red rectangle
882 every time where the amplitude is higher than a threshold of 0.5 mm (for
883 the GPS) or 0.01 (for the tremor, **that is about 56 times the average**
884 **value of the signal)**. We mark by a blue rectangle every time where the
885 amplitude is lower than minus the threshold.

886 ● Figure 7. Top: Stacked 6th level details of the wavelet decomposition of
887 the displacement over all the GPS stations located in a 50 km radius of a
888 given point, for the 16 red triangles indicated in Figure 3. Bottom: 6th
889 level detail multiplied by -1 of the cumulative tremor count in a 50 km
890 radius of a given point for the same 16 locations. The black lines represent
891 the timings of the ETS events from Table 1. We mark by a red rectangle
892 every time where the amplitude is higher than a threshold of 0.3 mm (for
893 the GPS) or 0.009 (for the tremor, **that is about 51 times the average**
894 **value of the signal)**. We mark by a blue rectangle every time where the
895 amplitude is lower than minus the threshold.

896 ● Figure 8. ROC curve for the sum of the 6th, 7th, and 8th level details
897 of the wavelet decomposition. Each dot represents the true positive rate
898 of event detections and the false positive rate of event detections for a
899 given pair of thresholds (for the GPS and for the tremor). The black
900 cross marks the true positive rate and the false positive rate obtained

901 with the thresholds used to make Figure 9. The values of the threshold
902 are color-coded. Reds (bottom curve) correspond to the lowest value of
903 the threshold for the tremor (0.001), while oranges, greens, blues, purples
904 correspond to increasing values of the threshold for the tremor (up to 0.01,
905 top curve). The brightest colors (bottom left) correspond to the highest
906 values of the threshold for the GPS (1.5 mm), while the darker colors (top
907 right) correspond to decreasing values of the threshold for the GPS (0.1
908 mm).

- 909 • Figure 9. Top: Stacked sum of the 6th, 7th and 8th levels details of
910 the wavelet decomposition of the displacement over all the GPS stations
911 located in a 50 km radius of a given point, for the 16 red triangles indicated
912 in Figure 3. Bottom: Sum of the 6th, 7th and 8th levels detail multiplied
913 by -1 of the cumulative tremor count in a 50 km radius of a given point
914 for the same 16 locations. The black lines represent the timings of the
915 ETS events from Table 1. We mark by a red rectangle every time where
916 the amplitude is higher than a threshold of 0.8 mm (for the GPS) or 0.01
917 (for the tremor, **that is about 56 times the average value of the**
918 **signal**). We mark by a blue rectangle every time where the amplitude is
919 lower than minus the threshold.
- 920 • Figure 10. Top: Stacked 5th level details of the wavelet decomposition
921 of the displacement over all the GPS stations located in a 50 km radius
922 of a given point, for the 16 red triangles indicated in Figure 3. The red
923 lines represent the timings of the ETS events from Table 1. The blue
924 lines represent the timings of the magnitude 5 events from the catalog of
925 Michel et al. (2019).
- 926 • Figure 11. Same as top panel of Figure 9: Stacked sum of the 6th, 7th
927 and 8th levels details of the wavelet decomposition of the displacement

928 over all the GPS stations located in a 50 km radius of a given point, for
929 the 16 red triangles indicated in Figure 3. We mark with a green bar the
930 slow slip events from Table 4 detected with the wavelet method. Full lines
931 correspond to robust detections (1 in Table 4) and dotted lines to less
932 robust detections (2 in Table 4).

- 933 • Figure 12. GPS stations used for the slow slip detection in New Zealand
934 (black triangles). The red triangles are the locations where we stack the
935 GPS data. They are located close to the 20 km depth contour of the plate
936 boundary from Williams et al. (2013).
- 937 • Figure 13. Top: Sum of the stacked 6th, 7th and 8th level details of
938 the wavelet decomposition of the displacement over all the GPS stations
939 located in a 50 km radius of a given point, for the 18 red triangles indicated
940 in Figure 12. The time period covered is 2010-2016. We mark by a red
941 rectangle every time where the amplitude is higher than a threshold equal
942 to 0.8 mm. We mark by a blue rectangle every time where the amplitude
943 is lower than minus the threshold. Bottom: Sum of the stacked 6th, 7th
944 and 8th level details of the wavelet decomposition. We mark with an
945 orange bar the slow slip events detected by Todd and Schwartz (2016)
946 and with a green bar the slow slip events from Table 5 detected with the
947 wavelet method. Full lines correspond to robust detections (1 in Table 5)
948 and dotted lines to less robust detections (2 in Table 5).
- 949 • Figure 14. Top: Sum of the stacked 6th, 7th and 8th level details of
950 the wavelet decomposition of the displacement over all the GPS stations
951 located in a 50 km radius of a given point, for the 18 red triangles indicated
952 in Figure 12. The time period covered in 2016-2022. We mark by a red
953 rectangle every time where the amplitude is higher than a threshold equal
954 to 0.8 mm. We mark by a blue rectangle every time where the amplitude

955 is lower than minus the threshold. We mark with a green bar the slow
956 slip events from Table 6 detected with the wavelet method. Full lines
957 correspond to robust detections (1 in Table 6) and dotted lines to less
958 robust detections (2 in Table 6).

₉₅₉ **Figures**

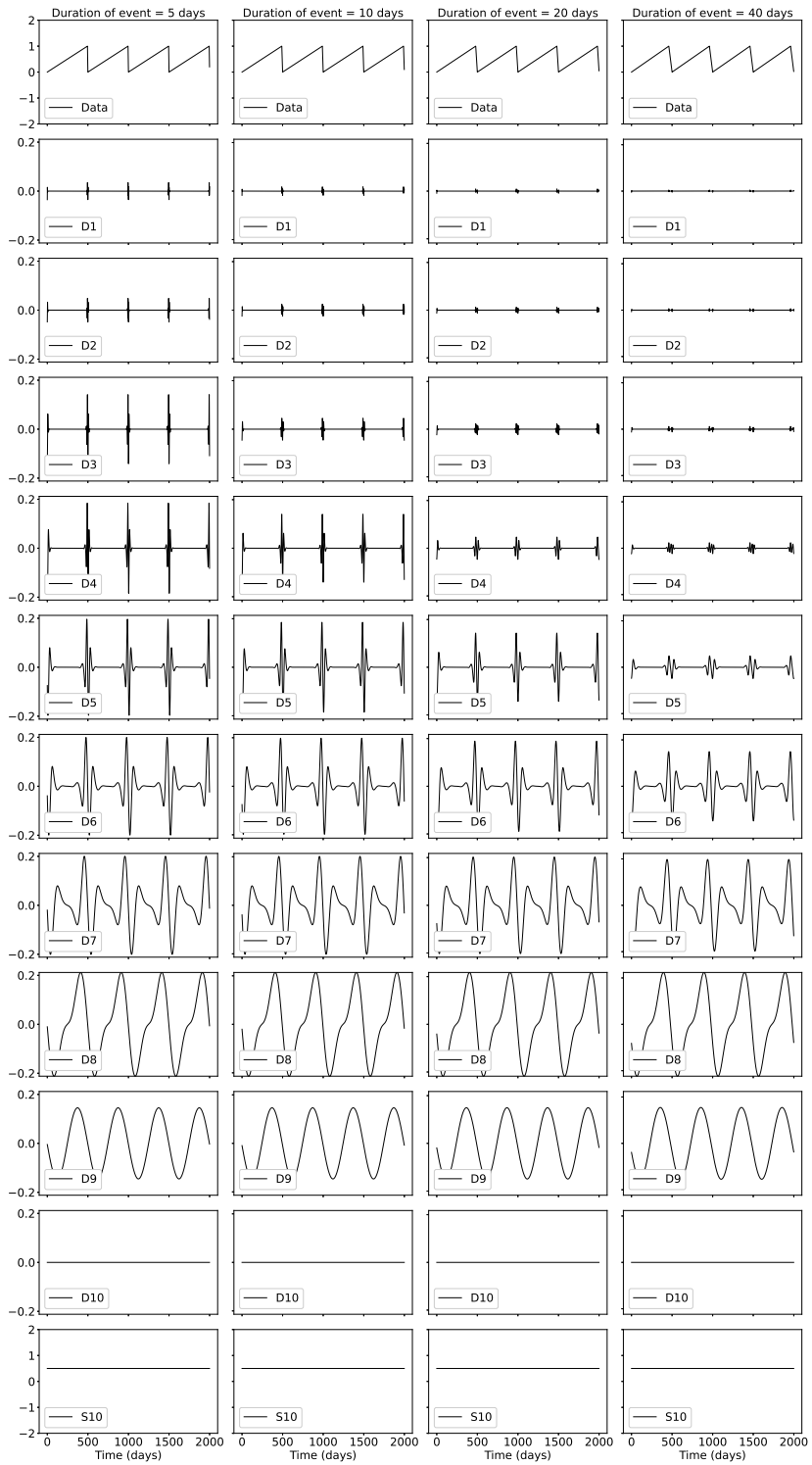


Figure 1: Demonstration of a wavelet decomposition for a synthetic dataset. A synthetic time series is created (top row) with steps of period 500 days, and transient durations of 2 days (left), 5 days, 10 days, and 20 days (right). The resulting details and smooths are shown in increasing level. The amplitude of the synthetic time series is normalized to 1, and the details and smooths show the relative amplitude. ⁴⁶

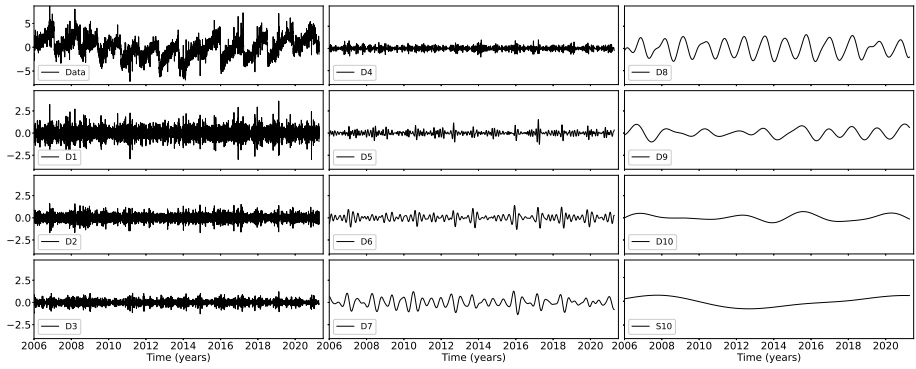


Figure 2: Top left: **East-west** displacement recorded at GPS station PGC5. The resulting details and smooth of the wavelet decomposition are shown in increasing level from top to bottom and from left to right.

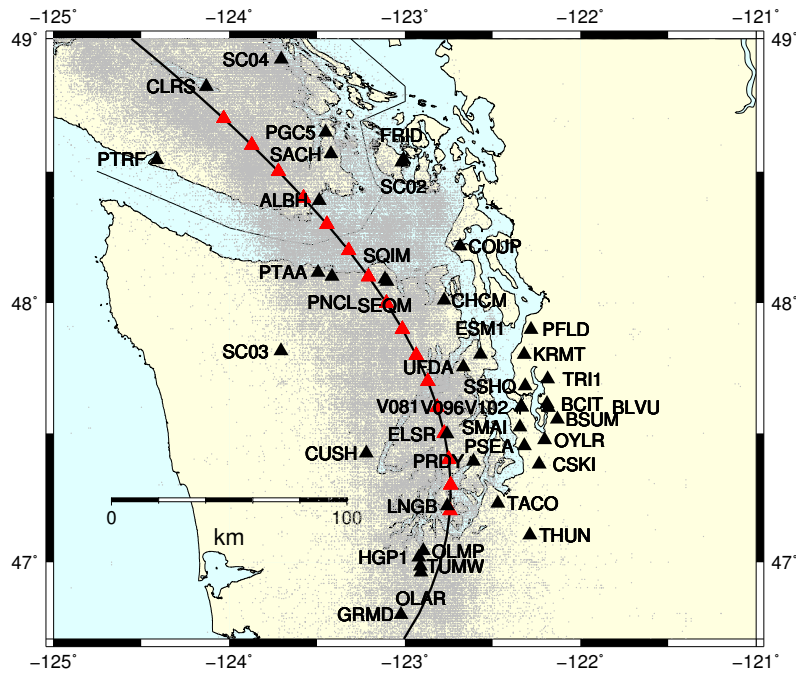


Figure 3: GPS stations used in this study (black triangles). The black line represents the 40 km depth contour of the plate boundary model by Preston et al. (2003). The red triangles are the locations where we stack the GPS data. The small grey dots are all the tremor locations from the PNSN catalog.

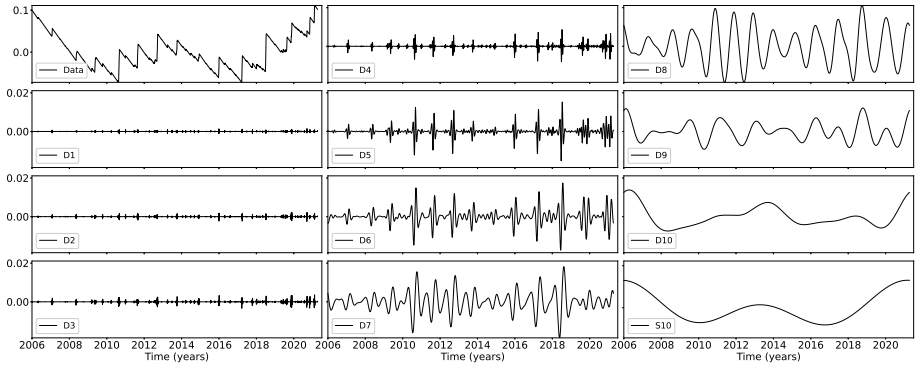


Figure 4: Details and smooth of the wavelet decomposition of the detrended cumulative tremor count around the third northernmost red triangles on Figure 3 (latitude 48.5).

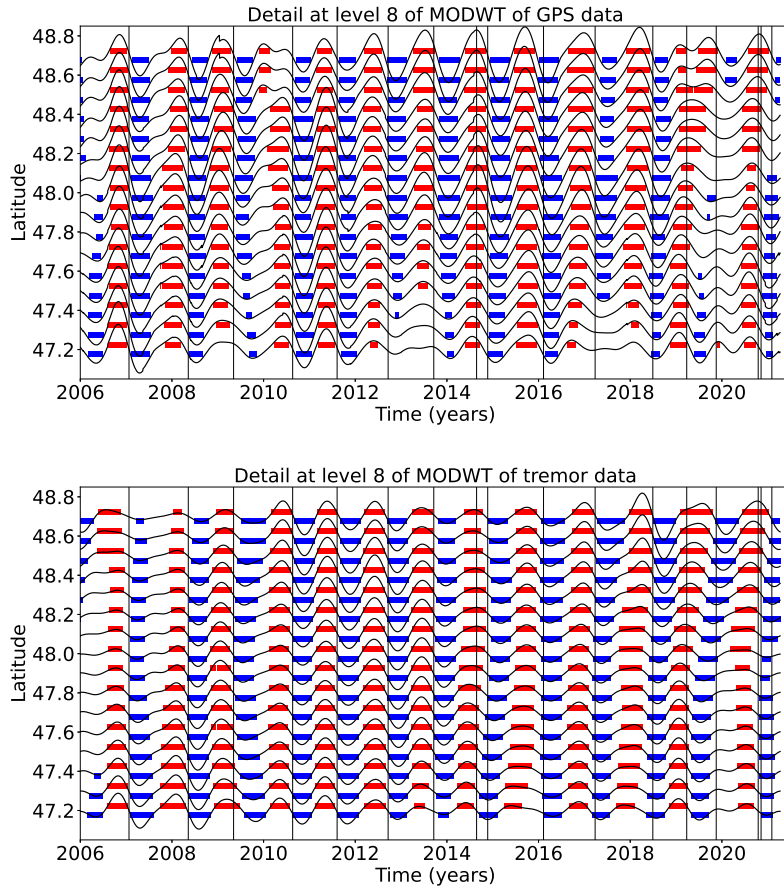


Figure 5: Top: Stacked 8th level details of the wavelet decomposition of the displacement over all the GPS stations located in a 50 km radius of a given point, for the 16 red triangles indicated in Figure 3. Bottom: 8th level detail multiplied by -1 of the cumulative tremor count in a 50 km radius of a given point for the same 16 locations. The black lines represent the timings of the ETS events from Table 1. We mark by a red rectangle every time where the amplitude is higher than a threshold of 0.4 mm (for the GPS) or 0.003 (for the tremor, **that is about 17 times the average value of the signal**). We mark by a blue rectangle every time where the amplitude is lower than minus the threshold.

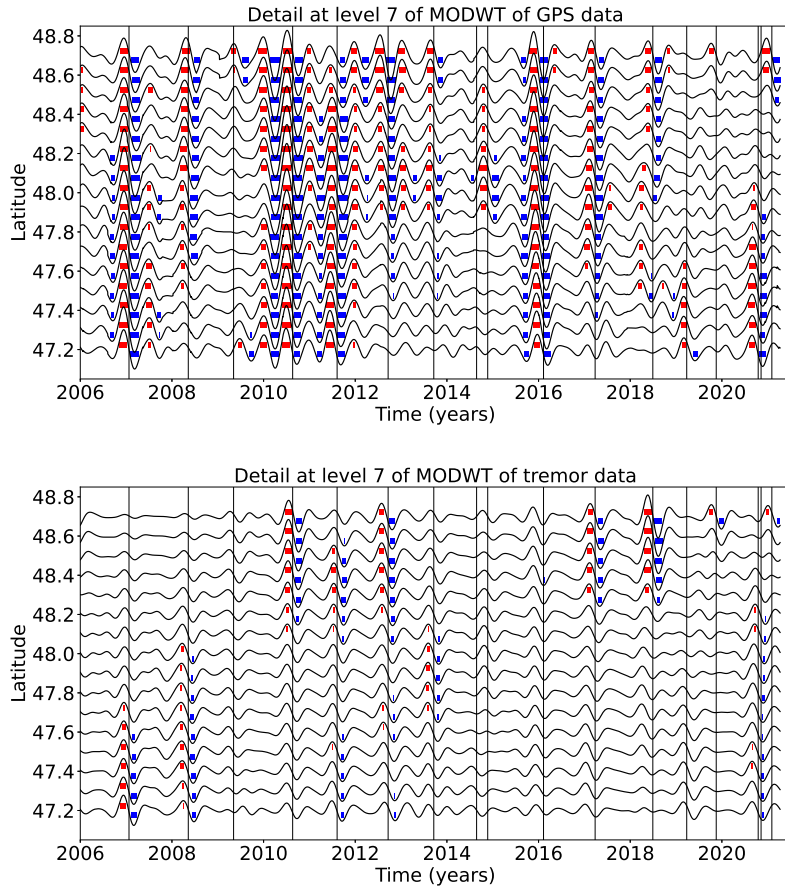


Figure 6: Top: Stacked 7th level details of the wavelet decomposition of the displacement over all the GPS stations located in a 50 km radius of a given point, for the 16 red triangles indicated in Figure 3. Bottom: 7th level detail multiplied by -1 of the cumulative tremor count in a 50 km radius of a given point for the same 16 locations. The black lines represent the timings of the ETS events from Table 1. We mark by a red rectangle every time where the amplitude is higher than a threshold of 0.5 mm (for the GPS) or 0.01 (for the tremor, **that is about 56 times the average value of the signal**). We mark by a blue rectangle every time where the amplitude is lower than minus the threshold.

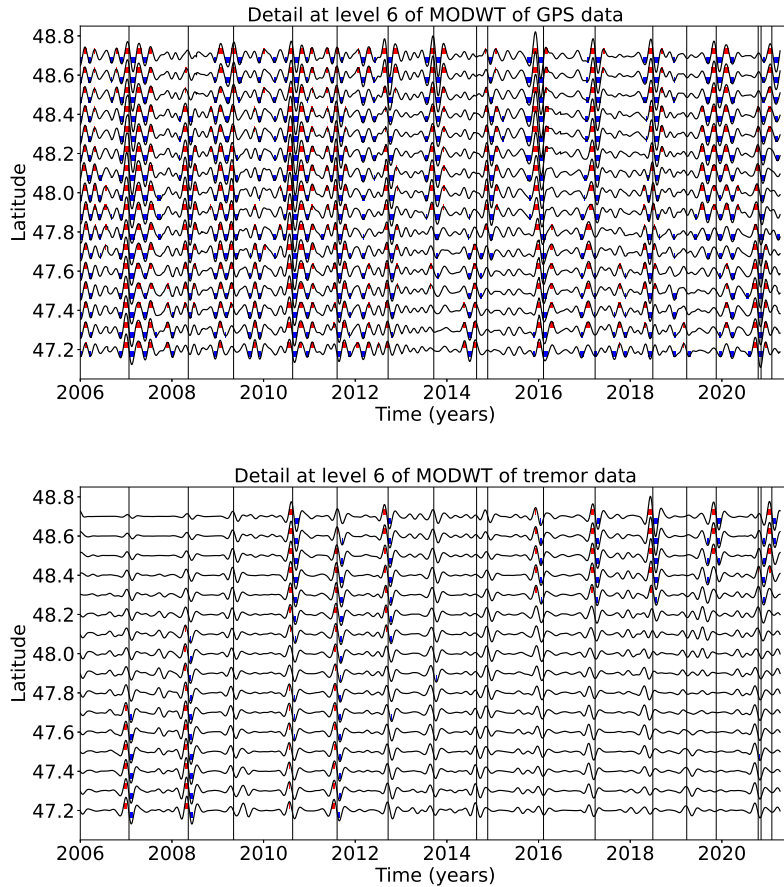


Figure 7: Top: Stacked 6th level details of the wavelet decomposition of the displacement over all the GPS stations located in a 50 km radius of a given point, for the 16 red triangles indicated in Figure 3. Bottom: 6th level detail multiplied by -1 of the cumulative tremor count in a 50 km radius of a given point for the same 16 locations. The black lines represent the timings of the ETS events from Table 1. We mark by a red rectangle every time where the amplitude is higher than a threshold of 0.3 mm (for the GPS) or 0.009 (for the tremor, **that is about 51 times the average value of the signal**). We mark by a blue rectangle every time where the amplitude is lower than minus the threshold.

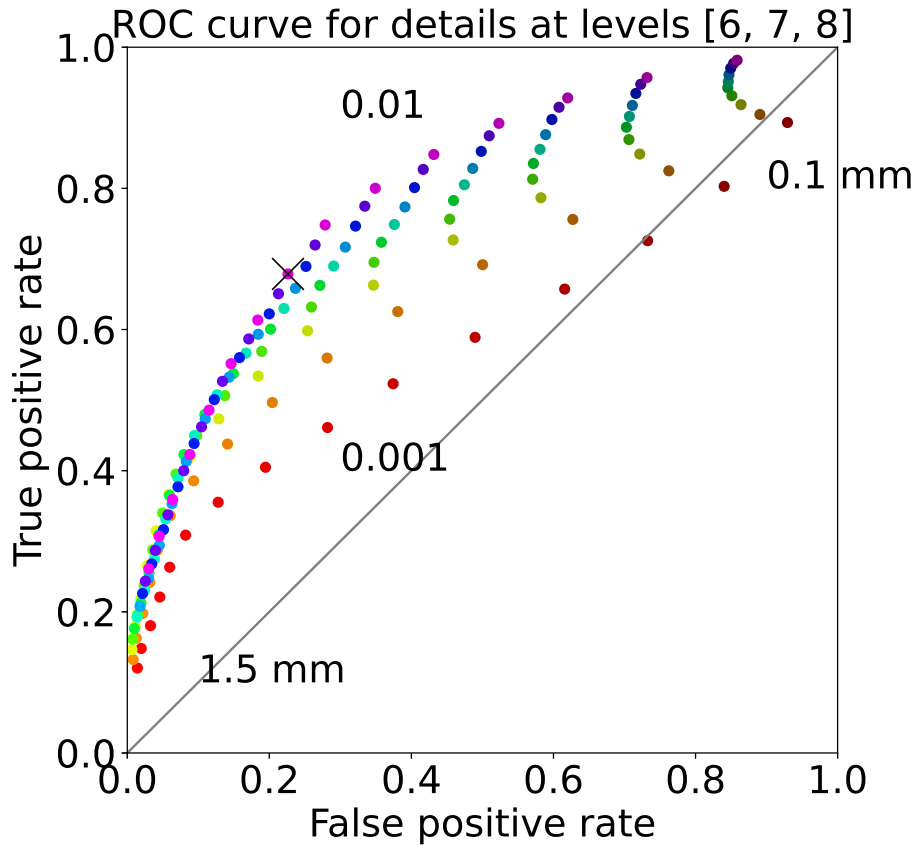


Figure 8: ROC curve for the sum of the 6th, 7th, and 8th level details of the wavelet decomposition. Each dot represents the true positive rate of event detections and the false positive rate of event detections for a given pair of thresholds (for the GPS and for the tremor). The black cross marks the true positive rate and the false positive rate obtained with the thresholds used to make Figure 9. The values of the threshold are color-coded. Reds (bottom curve) correspond to the lowest value of the threshold for the tremor (0.001), while oranges, greens, blues, purples correspond to increasing values of the threshold for the tremor (up to 0.01, top curve). The brightest colors (bottom left) correspond to the highest values of the threshold for the GPS (1.5 mm), while the darker colors (top right) correspond to decreasing values of the threshold for the GPS (0.1 mm).

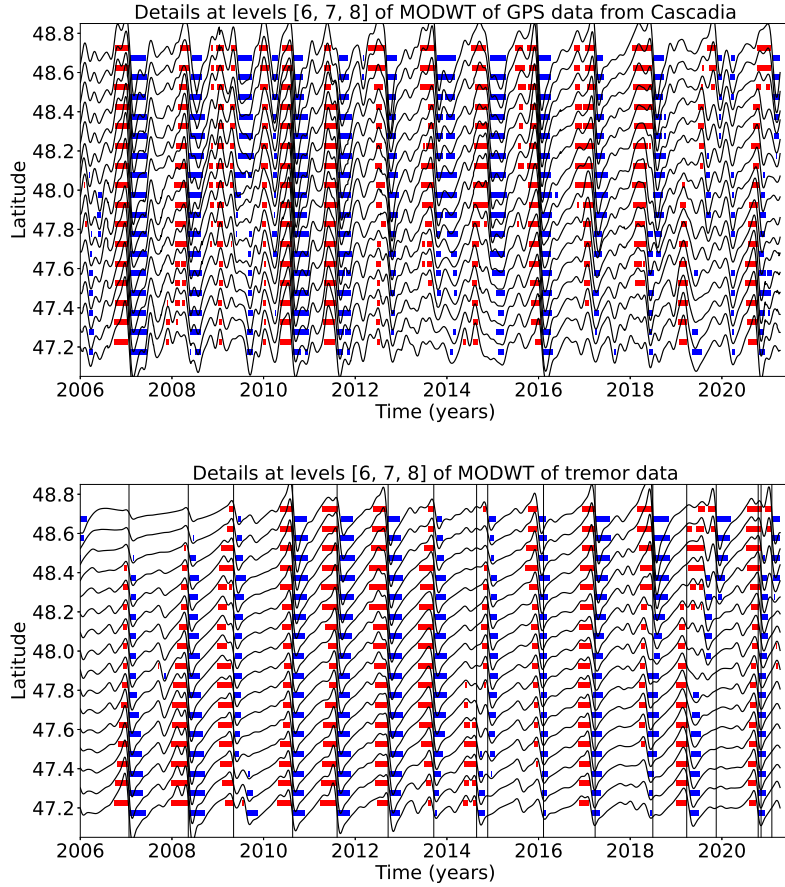


Figure 9: Top: Stacked sum of the 6th, 7th and 8th levels details of the wavelet decomposition of the displacement over all the GPS stations located in a 50 km radius of a given point, for the 16 red triangles indicated in Figure 3. Bottom: Sum of the 6th, 7th and 8th levels detail multiplied by -1 of the cumulative tremor count in a 50 km radius of a given point for the same 16 locations. The black lines represent the timings of the ETS events from Table 1. We mark by a red rectangle every time where the amplitude is higher than a threshold of 0.8 mm (for the GPS) or 0.01 (for the tremor, **that is about 56 times the average value of the signal**). We mark by a blue rectangle every time where the amplitude is lower than minus the threshold.

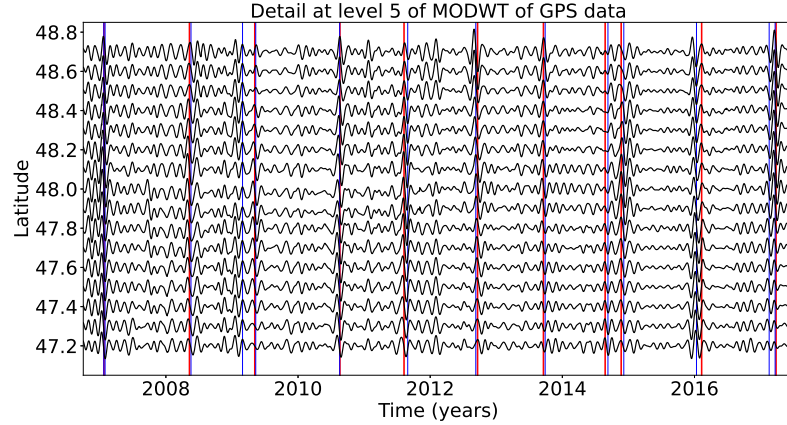


Figure 10: Top: Stacked 5th level details of the wavelet decomposition of the displacement over all the GPS stations located in a 50 km radius of a given point, for the 16 red triangles indicated in Figure 3. The red lines represent the timings of the ETS events from Table 1. The blue lines represent the timings of the magnitude 5 events from the catalog of Michel et al. (2019).

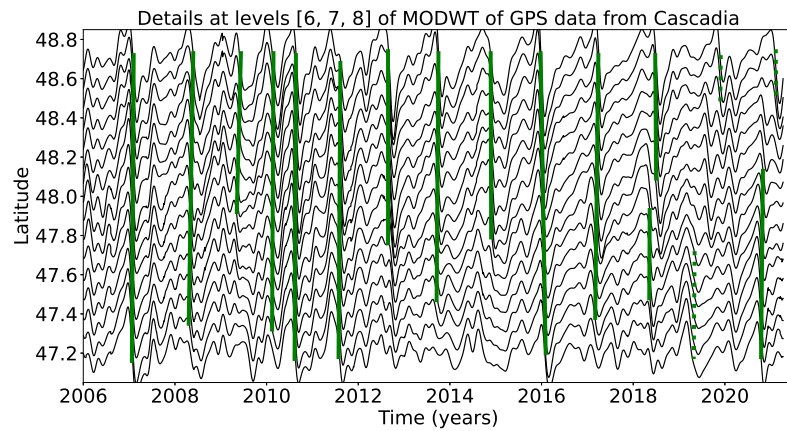


Figure 11: Same as top panel of Figure 9: Stacked sum of the 6th, 7th and 8th levels details of the wavelet decomposition of the displacement over all the GPS stations located in a 50 km radius of a given point, for the 16 red triangles indicated in Figure 3. We mark with a green bar the slow slip events from Table 4 detected with the wavelet method. Full lines correspond to robust detections (1 in Table 4) and dotted lines to less robust detections (2 in Table 4).

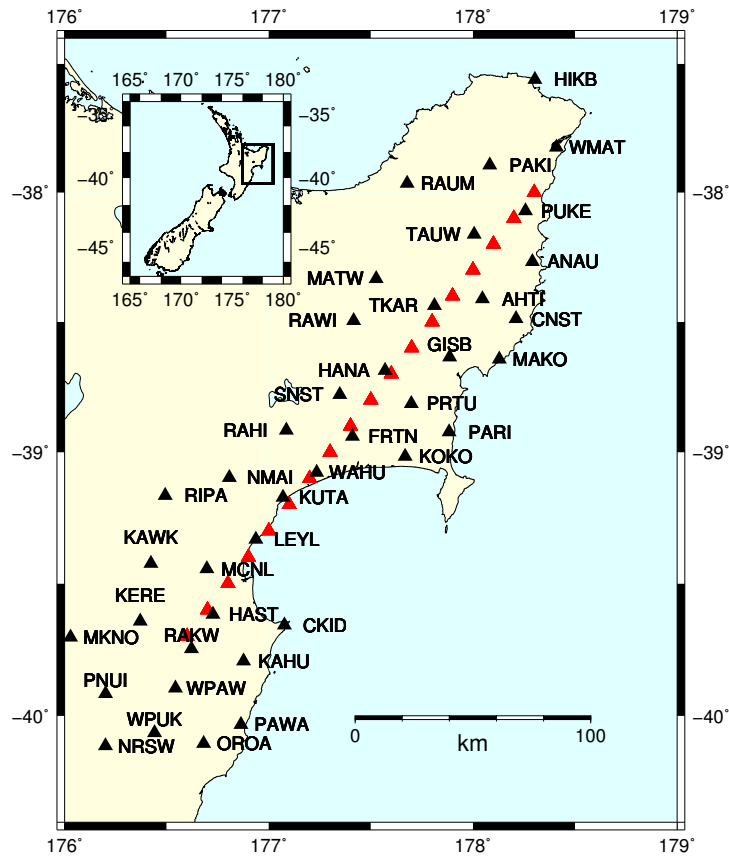


Figure 12: GPS stations used for the slow slip detection in New Zealand (black triangles). The red triangles are the locations where we stack the GPS data. They are located close to the 20 km depth contour of the plate boundary from Williams et al. (2013).

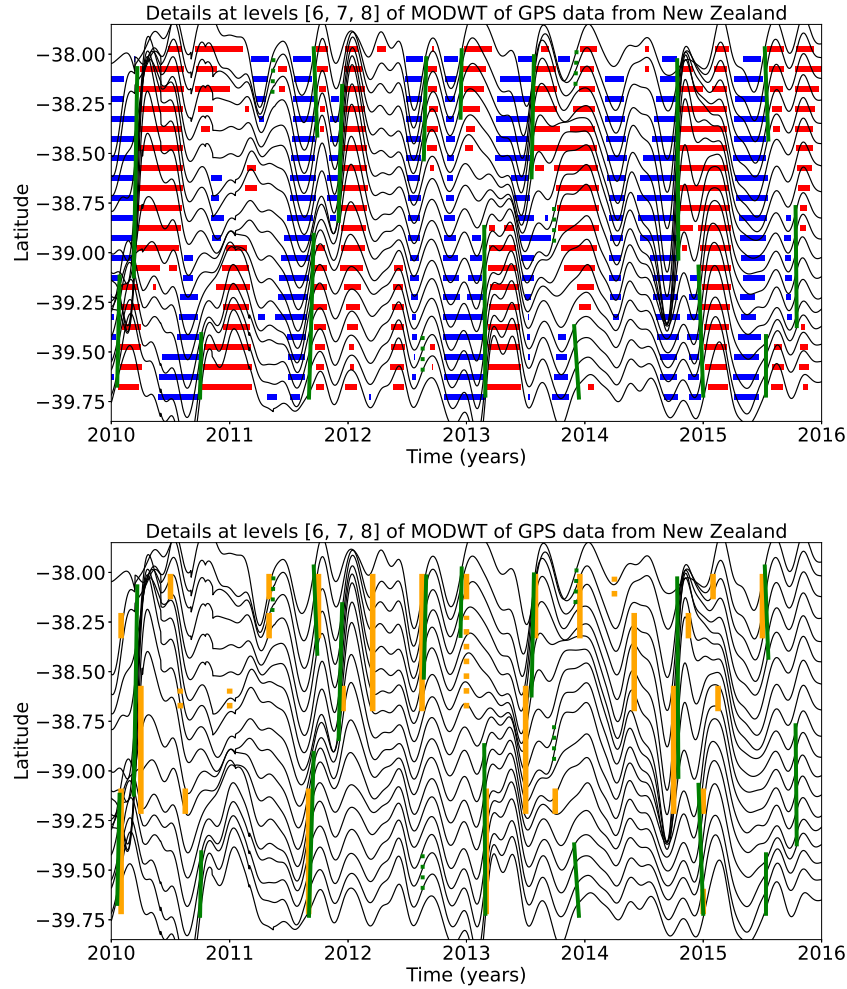


Figure 13: Top: Sum of the stacked 6th, 7th and 8th level details of the wavelet decomposition of the displacement over all the GPS stations located in a 50 km radius of a given point, for the 18 red triangles indicated in Figure 12. The time period covered is 2010-2016. We mark by a red rectangle every time where the amplitude is higher than a threshold equal to 0.8 mm. We mark by a blue rectangle every time where the amplitude is lower than minus the threshold. Bottom: Sum of the stacked 6th, 7th and 8th level details of the wavelet decomposition. We mark with an orange bar the slow slip events detected by Todd and Schwartz (2016) and with a green bar the slow slip events from Table 5 detected with the wavelet method. Full lines correspond to robust detections (1 in Table 5) and dotted lines to less robust detections (2 in Table 5).

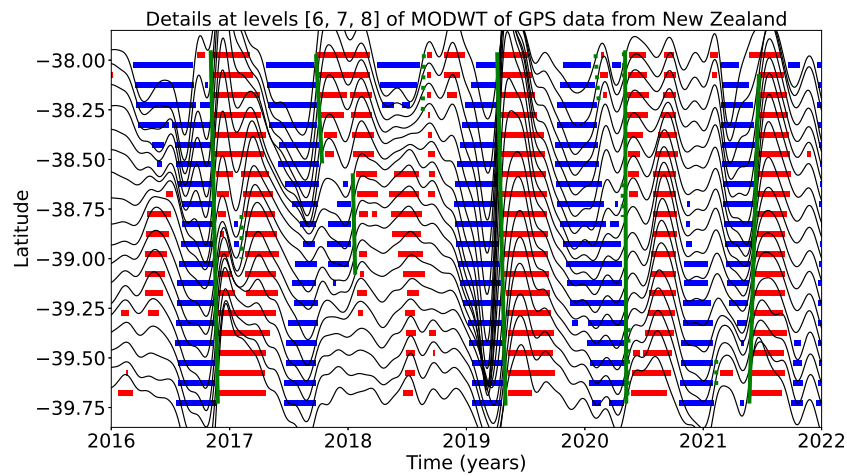


Figure 14: Top: Sum of the stacked 6th, 7th and 8th level details of the wavelet decomposition of the displacement over all the GPS stations located in a 50 km radius of a given point, for the 18 red triangles indicated in Figure 12. The time period covered in 2016-2022. We mark by a red rectangle every time where the amplitude is higher than a threshold equal to 0.8 mm. We mark by a blue rectangle every time where the amplitude is lower than minus the threshold. We mark with a green bar the slow slip events from Table 6 detected with the wavelet method. Full lines correspond to robust detections (1 in Table 6) and dotted lines to less robust detections (2 in Table 6).